

Trilayer Nanomesh Films with Tunable Wettability as Highly Transparent, Flexible, and Recyclable Electrodes

Tengfei Qiu, Bin Luo, Eser Metin Akinoglu, Jung-Ho Yun, Ian R. Gentle, and Lianzhou Wang*

Metallic mesh materials are promising candidates to replace traditional transparent conductive oxides such as indium tin oxide (ITO) that is restricted by the limited indium resource and its brittle nature. The challenge of metal based transparent conductive networks is to achieve high transmittance, low sheet resistance, and small perforation size simultaneously, all of which significantly relate to device performances in optoelectronics. In this work, trilayer dielectric/metal/dielectric (D/M/D) nanomesh electrodes are reported with precisely controlled perforation size, wire width, and uniform hole distribution employing the nanosphere lithography technique. $\text{TiO}_2/\text{Au}/\text{TiO}_2$ nanomesh films with small hole diameter (≤ 700 nm) and low thickness (≤ 50 nm) are shown to yield high transmittance ($>90\%$), low sheet resistance ($\leq 70 \Omega \text{ sq}^{-1}$), as well as outstanding flexural endurance and feasibility for large area patterning. Further, by tuning the surface wettability, these films are applied as easily recyclable flexible electrodes for electrochromic devices. The simple and cost-effective fabrication of diverse D/M/D nanomesh transparent conductive films with tunable optoelectronic properties paves a way for the design and realization of specialized transparent electrodes in optoelectronics.

storage devices, and bioelectronics, and are a key performance and a cost factor in these fast-growing markets.^[1,2] However, indium tin oxide (ITO), the most commonly employed transparent conductor in industry, does not meet the requirement of emerging flexible devices^[3] and is affected by the limited supply of indium. In recent years, different types of TCFs based on Mxene,^[4] graphene,^[5] carbon nanotubes,^[6] conductive polymers,^[7] metal nanowires,^[1] and patterned metallic meshes^[8–10] have been developed to replace ITO. Among these materials, patterned metallic meshes with nano or microstructured metallic networks fabricated by photolithography,^[11] inject printing,^[12] laser printing,^[13] and reverse-offset printing^[10] show great potential for application as high performance TCFs on account of both their performance and cost.^[14] Nevertheless, the patterns achieved by these methods possess relatively large pitch sizes, ranging from 10 μm to 5 mm, which affects the charge

collection efficiency within the network perforations. This inhomogeneity causes increased charge carrier recombination due to the increased in-plane charge diffusion pathway.^[8,15] Therefore, it is important to reduce the pitch size of these films.

Nanosphere lithography (NSL) utilizes a monolayer of close packed colloid particles as a template. As such, it is a unique and versatile technique for the fabrication of metal nanomesh electrodes with small perforation sizes in the order of hundreds of nanometers. Furthermore, NSL enables precise structural control and high uniformity of patterned films on both rigid and flexible substrates. In addition, this method is potentially scalable as the roll-to-roll fabrication of monolayer colloid particles has been realized^[16] and previously we have demonstrated highly ordered polystyrene (PS) particle monolayer arrays on 9 cm \times 9 cm polyethylene terephthalate (PET) substrates.^[17]


Metallic nanomesh electrodes fabricated by NSL exhibit distinct plasmonic properties including extraordinary transmission of light^[18] and surface plasmon resonances.^[19] These phenomena have been applied widely for sensors,^[20] solar cells,^[21] organic light emitting diodes (OLEDs),^[22] electrochromic devices,^[23] and transparent energy storage devices.^[17] Nevertheless, metallic nanomesh electrodes with ordered spherical perforations have been limited in their transparency, where engineering the mesh size for sufficiently small hole

1. Introduction

Transparent conductive films (TCFs) have been widely applied in both rigid and flexible optoelectronics including displays, solar cells, touch panels, smart windows, transparent energy

Dr. T. Qiu, Dr. B. Luo, Dr. J.-H. Yun, Prof. L. Wang
Nanomaterials Centre
School of Chemical Engineering and Australian Institute
for Bioengineering and Nanotechnology
The University of Queensland
St Lucia, QLD 4072, Australia
E-mail: l.wang@uq.edu.au

Dr. E. M. Akinoglu
ARC Centre of Excellence in Exciton Science
School of Chemistry
University of Melbourne
Parkville, VIC 3010, Australia
Prof. I. R. Gentle
School of Chemistry and Molecular Biosciences
Faculty of Science
The University of Queensland
St Lucia, QLD 4072, Australia

 The ORCID identification number(s) for the author(s) of this article can be found under <https://doi.org/10.1002/adfm.202002556>.

DOI: 10.1002/adfm.202002556

sizes yields transparencies below 80% as listed in Table S1 in the Supporting Information.

The main reason for the loss of transmittance is the unavoidable opaque metal shadow area, which occupies at least 9.3% of the total area due to the geometric limitations of a hexagonally close packed (hcp) monolayer of spherical particles.^[24] In addition, the excitation of surface plasmons unavoidably results in light absorption in those resonance conditions, and imperfections in the 2D ordering can increase the metallic opaque shadow areas. However, these factors can be engineered to have a minimal effect on the application at hand by tuning the plasmonic resonances outside of the significant spectrum and improving the quality of the mesh.

Previously we reported an approach to overcome the transmittance limitations and increase the transmittance from 37.5% to 80% at 550 nm by modifying the mesh-pattern shape from round holes to crosswires and thus removing the geometric limitations of hcp monolayers of spherical particles. To this end we used an angle resolved NSL technique which requires an extremely ordered particle array as a template.^[24] Bley et al. reported a hierarchical structure which comprises nanoholes (hole size 213 nm) on the metallic mesh (hole size 857 nm, periodicity 1500 nm) to decrease the metal coverage area and slightly increased the transmittance from 79% to 84%.^[25] However, fundamentally, this structure did not change the shape of the holes and did not overcome the geometric limitations. Wu and Tassi^[26] reported Ag/Al stacked nanomesh electrodes to reduce the reflection and absorption losses which mainly increased the transmittance in the long visible and near IR spectral range. Li et al. reported on ultrathin Au nanomesh electrodes at thicknesses below the characteristic skin depth of gold ≈ 25 nm, with a 2 nm thick Ti adhesion layer, and Gao et al. reported ultrathin Cu micromesh electrodes without an adhesion layer. Both of these studies achieved TCFs with transmittance close to 90%, however, their sheet resistance significantly increased upon mild bending or tape testing because the adhesion layer was very thin or missing. An ultrathin Cr, Ni, Ti, or Al layer (5–10 nm) is usually used as an adhesion layer between noble metal meshes and substrates,^[27] which however significantly affects the transmittance (Figure S1, Supporting Information). Further reducing the thickness would cause metal discontinuity as described in the Wolmer–Weber mechanism resulting in large sheet resistances.^[28] In this work, our strategy is to make the metal shadow area highly transparent by integrating a dielectric/metal/dielectric (D/M/D) antireflection system into the nanomesh structure. D/M/D material systems (D = TiO₂, WO₃, MoO₃, ZnS etc.; M = Ag, Au, Cu etc.), have been reported to efficiently increase the transmittance of a thin metal film through the induced transmittance effect.^[28,29,30] Even though D/M/D structures have been applied in mesoscale-patterned films,^[31] the D/M/D layered nanomesh structure for TCFs has not been explored before.

Here, we present a new class of D/M/D (D = TiO₂, M = Au, Ag) trilayer order nanomesh TCFs with spherical perforations and address their transmittance limitations. We use a TiO₂/Au/TiO₂ nanomesh as an example because Au is a widely applied electrode material and can meet multiple application requirements. The integration of two thin layers of TiO₂ with

thicknesses less than 15 nm significantly improves the transmittance and preserves the high conductivity and good flexibility of the metal mesh electrodes. We choose ultrathin TiO₂ layers to minimize the effect on the mechanical and electrical properties while reducing the material costs at the same time. Traditionally, 30 to 50 nm of TiO₂ layers were the optimized thickness for highly transparent D/M/D TCFs.^[30,32] As a result, we have achieved the TiO₂/Au/TiO₂ nanomesh TCFs with the highest transmittance over 90% and sheet resistance lower than 70 Ω sq⁻¹ simultaneously with the hole diameter smaller than 700 nm, which are among the best performance patterned TCFs. Moreover, the TiO₂/Au/TiO₂ nanomesh TCFs exhibit excellent mechanical stability and are suitable for facile patterning and flexible applications demonstrated with a 13 cm \times 8 cm patterned transparent and flexible circuit application. Importantly, these TCFs on PET substrate can be either hydrophilic or hydrophobic depending on the pattern size. The hydrophobic trilayer nanomesh electrode can be easily recycled by fast water and ethanol flushing, as demonstrated in an electrochromic device application. We also extended this work to fabricate TiO₂/Ag/TiO₂ nanomesh films and achieved similar optical and electrical performance, indicating that the simple and cost-effective synthesis technique is useful to prepare diverse D/M/D nanomesh TCFs.

2. Results and Discussion

The fabrication of the D/M/D (D = TiO₂, M = Au, Ag) nanomesh followed a standard NSL process as illustrated in Figure 1a. Compared with the fabrication process of metal nanomesh electrodes, the difference lies in the sequential deposition of TiO₂/metal/TiO₂ instead of metal. Therefore, this method is easy to manipulate and universal for the fabrication of multiple D/M/D nanomesh electrodes. In detail, firstly a hexagonally close packed monolayer of polystyrene particles with an initial diameter of 750 nm was self-assembled on the water surface forming a homogeneous film, and then deposited on a substrate.^[33] Next, PS particles were shrunk by reactive ion etching (RIE) to create a uniform non-close-packed particle monolayer as the mask for metal deposition. The hole size was controlled by adjusting the RIE time while keeping other parameters unchanged (Figure S2, Supporting Information). After that, a continuous electron beam evaporation process was used to deposit TiO₂, Au (or Ag) and TiO₂ onto the substrate without breaking vacuum. The broad peak in the X-ray diffraction (XRD) spectra represents the amorphous TiO₂ (Figure S3, Supporting Information). The thickness of the deposited films was measured in situ by a quartz crystal monitor, which was calibrated by atomic force microscopy (AFM).

The typical TiO₂/Au/TiO₂ nanomesh TCFs show light brown color with very high transparency (Figure 1b). Scanning electron microscope (Figure 1c) and microscope images (Figure S4, Supporting Information) show the morphology of a typical TiO₂/Au/TiO₂ nanomesh film with long-range ordered holes over 80 μ m \times 45 μ m area, indicating a high degree of uniformity of the films. The enlarged SEM image shows the smooth surface of the TiO₂/Au/TiO₂ nanomesh on glass substrate. The average

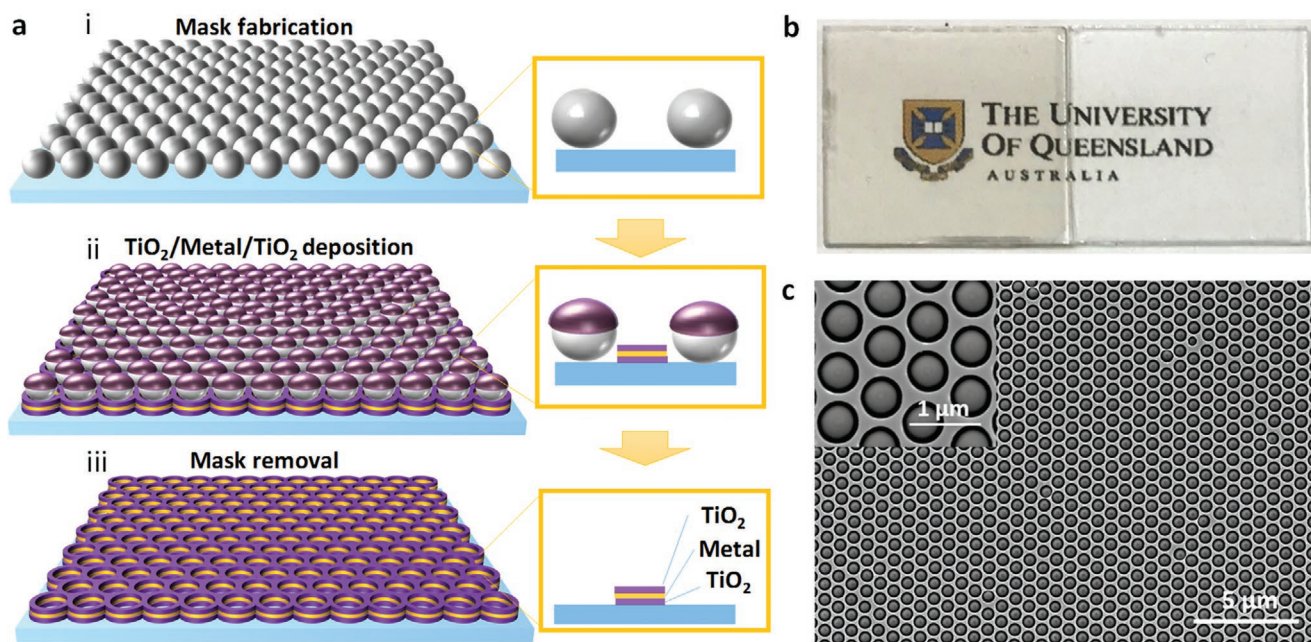


Figure 1. a) Schematic illustration for the fabrication of the D/M/D (D = TiO₂, M = Au, Ag, Cu) sandwich nanomesh-based TFCs. i) A monolayer of polystyrene (PS) particles is deposited on the substrate and etched by reactive ion etching (RIE) as the mask. ii) TiO₂, metal and TiO₂ are evaporated layer after layer without breaking vacuum. iii) The TiO₂/Metal/TiO₂ nanomesh films are obtained by removing the PS particles. b) Photographs of the TiO₂/Au/TiO₂ nanomesh on glass (left) and the glass substrate (right). A printed piece of paper is placed underneath to illustrate the transparency. c) Scanning electron microscopy (SEM) image of a typical TiO₂/Au/TiO₂ nanomesh film with the hole size of 650 nm on glass substrate. The insert is a partially enlarged view of (c).

roughness of the mesh shadow area is less than 1 nm measured from the AFM image of a typical TiO₂/Au/TiO₂ nanomesh with a thickness of 39 nm on the glass (Figure S5a, Supporting Information). The AFM image of a TiO₂/Au/TiO₂ nanomesh film as thin as 25 nm also shows very compact and smooth surface (Figure S5b, Supporting Information). The very smooth surface at very low metal thickness indicates the strong interfacial adhesion between TiO₂ and Au.^[28]

The effect of the integration of the D/M/D layered materials with the nanomesh structure with round holes on the transmittance was compared between typical TiO₂/Au/TiO₂ nanomesh films and pure Au nanomesh films in **Figure 2**. The TiO₂/Au/TiO₂ films and the Au films had the same Au thickness in these experiments (Figure 2a). For the Au film and the Au nanomesh, a layer of 5 nm Ti was applied as the adhesion layer. The TiO₂/Au/TiO₂ nanomesh shows greatly improved transmittance over the visible range among the listed TFCs due to the combination of the antireflective D/M/D construction as well as the patterned nanomesh structure. Compared with the Au nanomesh, by simply introducing two layers of 8 nm TiO₂ the transmittance (at 550 nm) is increased from 62.0% to 86.4%, indicating that the metal shadow area becomes more transparent, which is confirmed by the experimental and calculated spectra (Figure 2b) of the TiO₂/Au/TiO₂ and the Au films. The experimental data fit well with the calculated spectra and the slight difference is likely due to deviations of the material optical constants from the literature values or a small thickness measurement error. The enhanced transmittance of D/M/D structures can be attributed to the antireflective effect^[34] and the suppression of surface plasmon (SP),^[30] when a dielectric film with high refractive

index is coated on the metal film. In addition, the spectral response (600–800 nm)^[24,35] caused by the coupling of the light to the metallic nanomesh with periodic holes, is not obvious, as large fraction of photons are transmitted, while in contrast, the transmittance minimum at around 670 nm was clearly seen for the Au nanomesh. Compared with the TiO₂/Au/TiO₂ films, the perforations on the D/M/D nanomesh with a coverage percentage of 58% significantly increase the transmittance (at 550 nm) from 74.0% to 86.4%. The transmittance is improved approximately in parallel over the measured wavelength range (300 to 900 nm). The TiO₂/Au/TiO₂ nanomesh adds the advantage of the D/M/D structure and that of the mesh structure together to yield a superior transmittance performance.

As NSL is applicable for the fabrication of multiple D/M/D structures, and because Au is an expensive resource, we also used a much more abundant silver, extended our work to fabricate TiO₂/Ag/TiO₂ nanomeshes (Figure S6, Supporting Information) and studied the optical performances (Figure S7, Supporting Information). For the Ag film and the Ag nanomesh, a layer of 5 nm Ti was also applied as the adhesion layer. The TiO₂/Ag/TiO₂ nanomesh shows even more obviously improved transmittance (91.2%) compared with Ag nanomesh (57.6%) and TiO₂/Ag/TiO₂ film (83.4%). This result further confirms the synergistic effect of these two structures.

To further evaluate the quality and performance of the TFCs, figure of merit (FoM) values are calculated by the equation^[8]

$$\frac{\sigma_{\text{dc}}}{\sigma_{\text{opt}}} = \frac{188.5}{R_{\text{sheet}} \left(T_{550 \text{ nm}}^{-\frac{1}{2}} - 1 \right)} \quad (1)$$

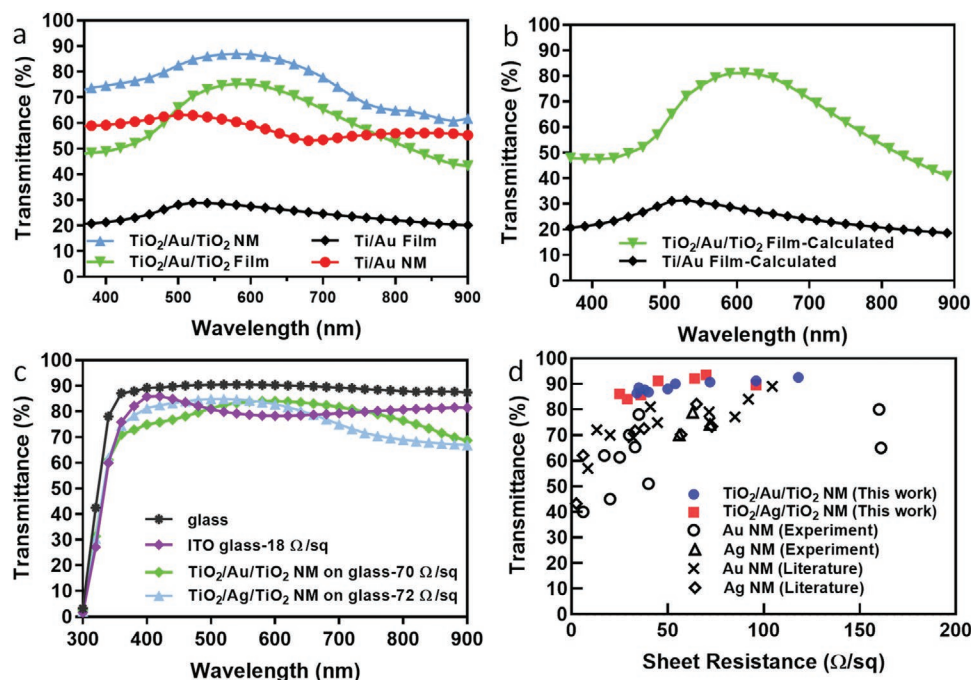


Figure 2. a) The transmittance spectra of the TiO₂/Au/TiO₂ film, the Au film and the corresponding nanomesh (NM). All the samples were with same Au thickness of 15 nm. The thickness of TiO₂ was 12 nm in TiO₂/Au/TiO₂ system, while 5 nm Ti was applied as the adhesion layer for Au films and Au nanomeshes in Ti/Au system. The nanomeshes are of average periodicity of 750 nm and average hole size of 600 nm. Transmission excludes substrate absorption, which was subtracted using a blank substrate. b) The calculated spectra of the TiO₂/Au/TiO₂ film (10 nm/15 nm/10 nm) and the Ti/Au film (5 nm/15 nm). c) Comparisons of the transmittance spectra of the glass, ITO on glass, TiO₂/Au/TiO₂ nanomesh, TiO₂/Ag/TiO₂ nanomesh on glass. Transmittance includes substrate absorption. d) Comparisons of sheet resistance versus transmittance of TiO₂/Au/TiO₂ and TiO₂/Ag/TiO₂ nanomesh films prepared in this work with Au and Ag nanomesh with similar pattern size by experiments or in literature (listed in Table S1, Supporting Information).

where σ_{dc} is direct current conductivity and σ_{opt} is the optical conductivity at a wavelength of 550 nm. Higher σ_{dc}/σ_{opt} value means a better transmittance-sheet resistance performance of the TCFs. We simply optimized the transmittance and sheet resistance trade off by adjusting the thicknesses of the TiO₂ and Au/Ag layers as well as the hole size. The transmittance of the films increases with the increase of TiO₂ thickness (Figure S8, Supporting Information), hole size and the decrease of metal thickness. The transmittance maximum shifts by changing the thicknesses. The sheet resistance is determined by the metal core and decreases with the increase of metal thickness and the decrease of hole size. The FoM values are the results of all these factors. The σ_{dc}/σ_{opt} values of these trilayer TCFs are generally between 40 and 100 (Table S2, Supporting Information). The TiO₂/Au/TiO₂ nanomesh with sheet resistance of 30 Ω sq⁻¹ at the transmittance of 88.4% (thickness 8 nm/16 nm/8 nm, hole size 650 nm) achieved the highest σ_{dc}/σ_{opt} of 98.8. And the TiO₂/Ag/TiO₂ nanomesh with sheet resistance of 70 Ω sq⁻¹ at the transmittance of 93.5% (thickness 12 nm/12 nm/12 nm, hole size 650 nm) achieved the highest σ_{dc}/σ_{opt} of 76.6. We show the typical transmittance curves of the TiO₂/Au/TiO₂ and TiO₂/Ag/TiO₂ nanomesh films compared with commercial ITO on glass substrates with the substrate absorption included (Figure 2c). All of them display comparable or even better transmittance in the visible region compared with ITO. Compared with our experimental and other published metal nanomesh TCFs (Table S1, Supporting Information), the

D/M/D nanomesh shows better transmittance-sheet resistance trade-off as shown in Figure 2d. These values are comparable to or higher than many previously reported values for currently available TCFs including ITO, metal grids,^[36] graphene,^[37] and carbon nanotubes.^[6] The FoMs of these films satisfy the industry requirement where $T > 90\%$ and $R < 100 \Omega \text{ sq}^{-1}$ and can be applied in multiple industry applications.^[38] Better performance can be expected by further optimizing the e-beam evaporation parameters to achieve higher quality films or by adjusting the periodicity of the holes.

TiO₂/Au/TiO₂ nanomesh and TiO₂/Ag/TiO₂ nanomesh exhibited transmittance-sheet resistance performances at similar levels, though at the same thickness, TiO₂/Au/TiO₂ nanomesh showed lower transmittance than TiO₂/Ag/TiO₂ nanomesh. This is expected because Ag has a lower refractive index n (0.059 at 550 nm) than Au (0.42 at 550 nm)^[39] and the photon energy absorbed by a metal layer is proportional to $nk d/\lambda$, where λ is the wavelength of incident light, k is the extinction coefficient, and d is the thickness of the metal film. However, from SEM images (Figure 1c), no grain boundary and pinhole was observed on the smooth TiO₂/Au/TiO₂ nanomesh surface even with the Au layer as thin as 8 nm, while these defects were clearly observed on TiO₂/Ag/TiO₂ nanomesh film (Figure S9, Supporting Information), slightly affecting both the transmittance and sheet resistance. In addition, the roughness of the mesh shadow area of the TiO₂/Au/TiO₂ nanomesh film was lower than that of the TiO₂/Ag/TiO₂ nanomesh film

(Figure S10, Supporting Information). These results additionally indicate the TiO_2/Au interface has lower interfacial free energy and higher interfacial adhesion compared with the TiO_2/Ag interface.

Further, to assess the mechanical properties, we fabricated trilayer nanomesh films on PET substrate and investigated the bending durability. Figure 3a shows the sheet resistance change of the $\text{TiO}_2/\text{Au}/\text{TiO}_2$ nanomesh films compared with commercially available ITO after one time bending and recovering at each bending radius. The sheet resistance of $\text{TiO}_2/\text{Au}/\text{TiO}_2$ nanomesh remained unchanged up to a bending radius of 1.5 mm. Even at a bending radius of 0.5 mm, the sheet resistance only rose by a factor of 2.7, which was similar to our previously reported Au grid films.^[36] At a bending radius of 2.5 mm, after 1000 cycles of bending, the sheet resistance of the $\text{TiO}_2/\text{Au}/\text{TiO}_2$ nanomesh remained unchanged, and very few cracks were observed on the nanomesh surface (Figure S11, Supporting Information). The excellent bending resistance can be attributed to the good flexibility of both the nanomesh^[40] and the D/M/D structures.^[30] The metal nanomesh combines the ductility of metal and the deformability of the nanomesh.^[41] In particular, oxygenated functional groups on the PET surface were induced during oxygen plasma (RIE) treatment, which then bonded with the TiO_2 layer effectively enhancing the mechanical properties.^[42] The tri layer nanomesh based on Ag exhibits less resistance to bending (Figure S12a,b, Supporting Information). The sheet resistance remained unchanged up to a bending radius of 1.5 mm after one time bending and recovering indicating good flexibility of the Ag nanomesh and the minimal effect of the TiO_2 layers. However, under a bending radius of 2.5, after 500 times bending, the $\text{TiO}_2/\text{Ag}/\text{TiO}_2$

nanomesh film failed during the sheet resistance measurement, indicating complete structure damage. Probable reasons are the aforementioned interfacial defects and inferior interfacial adhesion between Ag and TiO_2 . In contrast, at the bending radius of 6 mm, the sheet resistance of the ITO film started to increase, due to the generation and propagation of cracks on the PET substrate (Figure S11, Supporting Information). After 500 bending tests, a 60-fold times increase of the sheet resistance was observed on ITO. Moreover, we also performed the tape adhesion test, in which we apply a 3M Scotch tape onto the nanomesh with finger pressure before pulling it off to assess the adhesion of the $\text{TiO}_2/\text{Au}/\text{TiO}_2$ nanomesh (Figure 3c) and $\text{TiO}_2/\text{Ag}/\text{TiO}_2$ nanomesh (Figure S12c, Supporting Information) to the PET and glass substrates. No obvious sheet resistance change was observed for all samples, indicating strong adhesion forces between TiO_2 and the substrates.

Finally, we used $\text{TiO}_2/\text{Au}/\text{TiO}_2$ nanomesh as an example to demonstrate the application of these trilayer films. Flexible and transparent circuits are emerging in a wide range of applications such as displays, defogging systems, electromagnetic shielding, sensors, and electronic skins. It remains challenging to satisfy simultaneously the large-area and precisely tuning of transmittance and conductivity, flexibility and adhesion to substrate.^[43] We fabricated a 13 cm \times 8 cm transparent and flexible circuit with two kangaroo-shaped patterns of $\text{TiO}_2/\text{Au}/\text{TiO}_2$ nanomesh and successfully lit a blue LED, indicating the practicability of these TCFs in transparent circuit applications. The $\text{TiO}_2/\text{Au}/\text{TiO}_2$ nanomesh (15 nm/23 nm/15 nm) on PET has a high transmittance of 90% and sheet resistance of $62 \Omega \text{ sq}^{-1}$ (Figure S13, Supporting Information). The iridescence caused by the diffraction of light by the periodic nanomesh structures

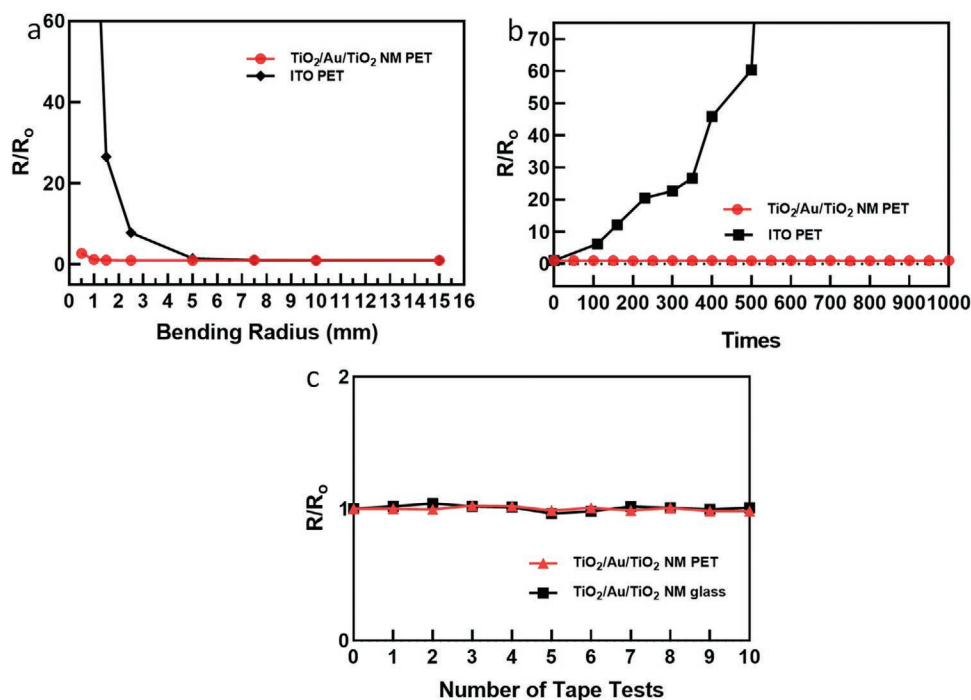


Figure 3. Sheet resistance change of the $\text{TiO}_2/\text{Au}/\text{TiO}_2$ nanomesh and ITO on PET substrates a) after one time bending and recovering at different bending radius, b) after 1000 times bending of these films, at a bending radius of 2.5 mm. c) Sheet resistance versus number of tape tests for $\text{TiO}_2/\text{Au}/\text{TiO}_2$ nanomesh on PET and glass substrate.

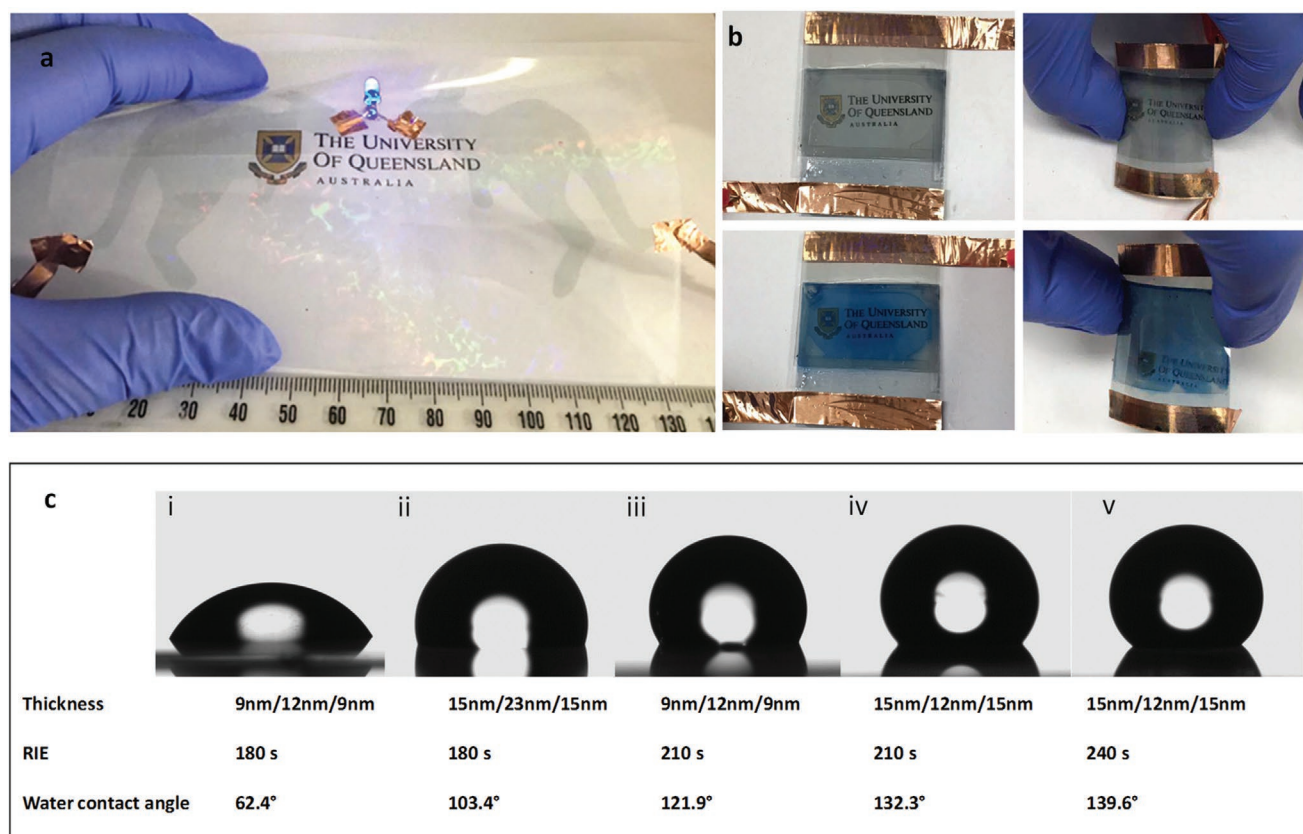


Figure 4. a) $\text{TiO}_2/\text{Au}/\text{TiO}_2$ nanomesh on PET substrate as a kangaroo-patterned transparent and flexible circuit to light up a blue LED. b) Left-side pictures are the color fading and color developing state of the electrochromic device with liquid electrolyte using $\text{TiO}_2/\text{Au}/\text{TiO}_2$ nanomesh as electrodes. Right side pictures are the color fading and color developing state of the flexible electrochromic device with solid gel electrolyte using the recycled $\text{TiO}_2/\text{Au}/\text{TiO}_2$ nanomesh as electrode. The papers with printed "The University of Queensland" are placed underneath to illustrate the transparency. c) Photos of the water droplets on the surface of $\text{TiO}_2/\text{Au}/\text{TiO}_2$ nanomeshes on PET substrates with corresponding parameters and water contact angles.

is clearly visible. This can be overcome by disturbing the periodicity of holes using a monolayer of aperiodic close-packed particle arrays (Figure S14, Supporting Information), as described in a previous work.^[23]

We also applied the $\text{TiO}_2/\text{Au}/\text{TiO}_2$ nanomesh films as recyclable electrodes for flexible electrochromic devices, where a layer of poly (3,4-ethylenedioxythiophene): poly (styrenesulfonate) (PEDOT: PSS) and a layer of electrolyte were sandwiched between two electrodes. With the extensive use of plastics, the landfill and incineration of plastic wastes seriously pollutes the natural environment. Therefore, developing renewable materials is significant for tackling waste disposal issues. One benefit of this nanomesh structure is that the water contact angle of the trilayer nanomesh is controllable from hydrophilic to hydrophobic (Figure 4c, 62.4° to 139.6°). Generally, reducing the hole diameter and increasing the mesh thickness will increase the water contact angle of the $\text{TiO}_2/\text{Au}/\text{TiO}_2$ nanomesh films owing to the increased roughness of the films. When we applied the hydrophobic nanomesh as the electrode in the electrochromic device, it was very easy to recycle. After 10 s of water and 5 s ethanol flushing, the electrode became very clean. We disassembled, washed, and reassembled the electrochromic devices 10 successive times and the electrode exhibited very good recyclability. The original electrochromic device with

liquid electrolyte and the electrochromic device with recycled electrode with solid electrolyte are shown in Figure 4b.

In summary, new D/M/D (D = TiO_2 , M = Au, Ag) trilayer nanomesh TCFs have been developed via a simple NSL approach and are demonstrated to be an effective solution to the low transmittance problem for nanohole arrays. The fabrication method is universal for the fabrication of multiple layered nanomesh materials. It is encouraging that the transmittance and sheet resistance performances of the $\text{TiO}_2/\text{Au}/\text{TiO}_2$ and $\text{TiO}_2/\text{Ag}/\text{TiO}_2$ sandwich nanomesh TCFs outperformed most of the reported TCFs with nanohole arrays. In particular, the $\text{TiO}_2/\text{Au}/\text{TiO}_2$ nanomesh shows good flexibility, great mechanical stability and is easily patterned and recycled. This work opens new opportunities for the design and fabrication of advanced optoelectronics.

3. Experimental Section

Preparation of D/M/D (D = TiO_2 , M = Au, Ag) Nanomesh Films: Firstly, the glass or PET substrates were immersed under water in a glass Petri dish. A monolayer of PS particles (750 nm, soap-free polymerization) was self-assembled at the water/air interface and consolidated to assure close packing.^[44] Then, the monolayer was deposited onto the substrates by pumping out the water followed by air-drying. Next, the substrates

were etched in a reactive ion etcher (RIE, Oxford Instruments Plasma Pro 80) at 60 W in 50 sccm O₂ to reduce PS particle size. Subsequently, TiO₂, Au (or Ag) and TiO₂ (Purity: 99.99%, Testbourne Ltd., UK) were deposited onto the substrate without breaking vacuum by e-beam evaporator (Temescal FC-2000). The evaporation rates for each layers were 1, 2, and 1 Å s⁻¹. The base pressure was less than 2.5 × 10⁻⁶ Torr. Substrate temperature was under 43 °C. The next step was to peel off the PS particles on top of the PET substrates with an adhesive tape. A plastic mask with two kangaroo-profile holes was placed on the substrates during the e-beam evaporation to fabricate the patterned TCF.

Material Characterization: The morphology, microstructure, and composition of the samples were investigated by field emission scanning electron microscope (FE-SEM, JEOL JSM-7100F), and AFM (Asylum Research Cypher AFM) measurements. The crystalline structure of the evaporated TiO₂ was examined with XRD (D8 Advance, Bruker). The water contact angles were measured on an optical contact angle instrument (OCA20, Dataphysics Instruments GmbH, Germany). The sheet resistances of the films were analyzed on a four-probe electroresistance analyzer (ST2258C). UV-vis absorption spectra were collected on a JASCOV-650 spectrophotometer in standard transmission geometry with unpolarized light. The reported sheet resistances and transmittances are the average values of the measurements.

Transmittance Spectra Calculation: The simulations were carried out with the COMSOL radio frequency (RF) model using a 2D model. The geometry of the model consists of unit cell with 5 μm height and 1 μm width. Periodic boundary conditions at the left and right boundaries insure continuity. The top boundary of the cell is the input port where wave excitation occurs with power = 1 W and electric field amplitude = 1 V m⁻¹, while the bottom boundary the detector port. The thin films were placed in the center of the cell height and the substrate was set to SiO₂,^[45] and the superstrate to air $n = 1$. The refractive index (dielectric permittivity) of the materials was obtained from literature, i.e., Ti, Cr, and Ni from,^[46] Ag and Au from,^[39] and TiO₂ from^[47]. The transmittance spectra were then obtained from the scattering matrix parameters of this finite-difference time-domain (FDTD) calculation.

Electrochromic Device Fabrication: Firstly, the gel electrolyte was prepared by mixing polyvinylpyrrolidone (PVP) (1.4 g), ethylene carbonate (EC) (2.5 g), lithium perchlorate (0.6 g) with ethanol (99.9%, 20 mL).

Then, a thin layer of PEDOT:PSS (Sigma-Aldrich, 0.5 wt% in 3:2 water/ethanol) was spin-coated onto a piece of TiO₂/Au/TiO₂ nanomesh film at 2000 rpm and dried on a heating stage at 90 °C for 5 min. Subsequently, another piece of the nanomesh film was pressed on top, applying Parafilm M sealing films at four edges as separator. Finally, the electrolyte solution was injected between the two films. The films were recycled by 10 s water flushing and 5 s ethanol flushing. Electrochromic devices with the recycled nanomesh films were fabricated in the following way. Firstly, a layer of PEDOT:PSS and a layer of gel electrolyte were in sequence spin-coated onto the nanomesh film as above described. Then it was covered with another piece of TiO₂/Au/TiO₂ nanomesh film and the two films were pressed together. The electrodes were recycled ten times.

Supporting Information

Supporting Information is available from the Wiley Online Library or from the author.

Acknowledgements

T.Q. and B.L. contributed equally to this work. The authors gratefully thank the Australian Research Council through its Discovery, DECRA (DE180100749) and Linkage (LP160100905) Programs. T.Q. thanks the financial support from the UQ Development fellowship (UQFEL1832321). E.M.A. acknowledges Feodor Lynen Research Fellowship by the Alexander

von Humboldt Foundation and funding by the Centre of Excellence in Exciton Science, Australian Research Council (CE170100026). This work was performed in part at the Queensland node of the Australian National Fabrication Facility, a company established under the National Collaborative Research Infrastructure Strategy to provide nano and microfabrication facilities for Australia's researchers. In addition, the authors acknowledge the facilities, and the scientific and technical assistance, of the Australian Microscopy & Microanalysis Research Facility at the Centre for Microscopy and Microanalysis, the University of Queensland.

Conflict of Interest

The authors declare no conflict of interest.

Keywords

electrochromic devices, flexible transparent conductive films, nanosphere lithography, recyclable electrodes, TiO₂/Au/TiO₂ nanomeshes, transparent circuits

Received: March 19, 2020

Revised: April 24, 2020

Published online: June 4, 2020

- [1] D. Li, W. Y. Lai, Y. Z. Zhang, W. Huang, *Adv. Mater.* **2018**, *30*, 1704738.
- [2] Y. Qiang, P. Artoni, K. J. Seo, S. Culacii, V. Hogan, X. Zhao, Y. Zhong, X. Han, P. M. Wang, Y. K. Lo, Y. Li, H. A. Patel, Y. Huang, A. Sambangi, J. S. V. Chu, W. Liu, M. Fagiolini, H. Fang, *Sci. Adv.* **2018**, *4*, eaat0626.
- [3] K. Alzoubi, M. M. Hamasha, S. Lu, B. Sammakia, *J. Disp. Technol.* **2011**, *7*, 593.
- [4] G. M. Weng, J. Li, M. Alhabeab, C. Karpovich, H. Wang, J. Lipton, K. Maleski, J. Kong, E. Shaulsky, M. Elimelech, *Adv. Funct. Mater.* **2018**, *28*, 1803360.
- [5] Y. Ma, L. Zhi, *Small Methods* **2019**, *3*, 1800199.
- [6] B. W. Wang, S. Jiang, Q. B. Zhu, Y. Sun, J. Luan, P. X. Hou, S. Qiu, Q. W. Li, C. Liu, D. M. Sun, H. M. Cheng, *Adv. Mater.* **2018**, *30*, 1802057.
- [7] X. Hu, X. Meng, L. Zhang, Y. Zhang, Z. Cai, Z. Huang, M. Su, Y. Wang, M. Li, F. Li, X. Yao, F. Wang, W. Ma, Y. Chen, Y. Song, *Joule* **2019**, *3*, 2205.
- [8] H. B. Lee, W. Y. Jin, M. M. Ovhall, N. Kumar, J. W. Kang, *J. Mater. Chem. C* **2019**, *7*, 1087.
- [9] S. Chen, B. Shi, W. He, X. Wu, X. Zhang, Y. Zhu, S. He, H. Peng, Y. Jiang, X. Gao, Z. Fan, G. Zhou, J. M. Liu, K. Kempa, J. Gao, *Adv. Funct. Mater.* **2019**, *29*, 1906618.
- [10] J. Gao, Z. Xian, G. Zhou, J. M. Liu, K. Kempa, *Adv. Funct. Mater.* **2018**, *28*, 1705023.
- [11] Z. Zhong, K. Woo, I. Kim, H. Kim, P. Ko, D. Kang, S. Kwon, H. Kim, H. Youn, J. Moon, *Small* **2018**, *14*, 1800676.
- [12] W.-Y. Jin, R. T. Ginting, K.-J. Ko, J.-W. Kang, *Sci. Rep.* **2016**, *6*, 36475.
- [13] V. B. Nam, J. Shin, Y. Yoon, T. T. Giang, J. Kwon, Y. D. Suh, J. Yeo, S. Hong, S. H. Ko, D. Lee, *Adv. Funct. Mater.* **2019**, *29*, 1806895.
- [14] S. Chen, L. Song, Z. Tao, X. Shao, Y. Huang, Q. Cui, X. Guo, *Org. Electron.* **2014**, *15*, 3654.
- [15] D. Chen, G. Fan, H. Zhang, L. Zhou, W. Zhu, H. Xi, H. Dong, S. Pang, X. He, Z. Lin, *Nanomaterials* **2019**, *9*, 932.
- [16] X. Li, J. F. Gilchrist, *Langmuir* **2016**, *32*, 1220.

- [17] T. Qiu, B. Luo, M. Giersig, E. M. Akinoglu, L. Hao, X. Wang, L. Shi, M. Jin, L. Zhi, *Small* **2014**, *10*, 4136.
- [18] a) M. Couture, Y. Liang, H.-P. Poirier Richard, R. Faid, W. Peng, J.-F. Masson, *Nanoscale* **2013**, *5*, 12399; b) T. W. Ebbesen, H. J. Lezec, H. F. Chaemi, T. Thio, P. A. Wolff, *Nature* **1998**, *391*, 667.
- [19] T.-H. Park, N. Mirin, J. B. Lassiter, C. L. Nehl, N. J. Halas, P. Nordlander, *ACS Nano* **2008**, *2*, 25.
- [20] M. Weiler, C. Menzel, T. Pertsch, R. Alaee, C. Rockstuhl, C. Pacholski, *ACS Appl. Mater. Interfaces* **2016**, *8*, 26392.
- [21] C. Stelling, C. R. Singh, M. Karg, T. A. F. König, M. Thelakkat, M. Retsch, *Sci. Rep.* **2017**, *7*, 42530.
- [22] Y. H. Ho, K. Y. Chen, K. Y. Peng, M. C. Tsai, W. C. Tian, P. K. Wei, *Opt. Express* **2013**, *21*, 8535.
- [23] T. Qiu, B. Luo, F. Ali, E. Jaatinen, L. Wang, H. Wang, *ACS Appl. Mater. Interfaces* **2016**, *8*, 22768.
- [24] Q. Tengfei, A. E. Metin, L. Bin, G. Michael, L. Minghui, N. Jing, Z. Linjie, *Part. Part. Syst. Character.* **2017**, *34*, 1600262.
- [25] K. Bley, J. Semmler, M. Rey, C. Zhao, N. Martic, R. N. Klupp Taylor, M. Stingl, N. Vogel, *Adv. Funct. Mater.* **2018**, *28*, 1706965.
- [26] W. Wu, N. G. Tassi, *Nanoscale* **2014**, *6*, 7811.
- [27] P. Benjamin, C. Weaver, F. Mott Nevill, *Proc. R. Soc. London, Ser. A* **1962**, *261*, 516.
- [28] Y.-G. Bi, Y.-F. Liu, X.-L. Zhang, D. Yin, W.-Q. Wang, J. Feng, H.-B. Sun, *Adv. Opt. Mater.* **2019**, *7*, 1800778.
- [29] a) J. Zhou, Z. Wu, Z. Liu, *Rare Met.* **2008**, *27*, 457; b) P. C. Lansåker, J. Backholm, G. A. Niklasson, C. G. Granqvist, *Thin Solid Films* **2009**, *518*, 1225.
- [30] S. Kim, J.-L. Lee, *J. Photon Energy* **2012**, *2*, 021215.
- [31] a) C. T. Wang, C. C. Ting, P. C. Kao, S. R. Li, S. Y. Chu, *J. Appl. Phys.* **2017**, *122*, 085501; b) W.-K. Kim, S. Lee, D. Hee Lee, I. Hee Park, J. Seong Bae, T. Woo Lee, J.-Y. Kim, J. Hun Park, Y. Chan Cho, C. Ryong Cho, S.-Y. Jeong, *Sci. Rep.* **2015**, *5*, 10715; c) J. Huang, Y. Lu, W. Wu, J. Li, X. Zhang, C. Zhu, Y. Yang, F. Xu, W. Song, *J. Appl. Phys.* **2017**, *122*, 195302.
- [32] D. Kim, *Opt. Commun.* **2010**, *283*, 1792.
- [33] W. Kandulski, *PhD thesis*, Bonn University, xxx **2007**.
- [34] J. H. Kim, H.-K. Lee, J.-Y. Na, S.-K. Kim, Y.-Z. Yoo, T.-Y. Seong, *Ceram. Int.* **2015**, *41*, 8059.
- [35] J. F. Zhu, X. D. Zhu, R. Hoekstra, L. Li, F. X. Xiu, M. Xue, B. Q. Zeng, K. L. Wang, *Appl. Phys. Lett.* **2012**, *100*, 143109.
- [36] T. Qiu, B. Luo, M. Liang, J. Ning, B. Wang, X. Li, L. Zhi, *Carbon* **2015**, *81*, 232.
- [37] N. Jing, H. Long, J. Meihua, Q. Xiongying, S. Yudi, L. Jiaxu, Z. Xinghao, W. Bin, L. Xianglong, Z. Linjie, *Adv. Mater.* **2017**, *29*, 1605028.
- [38] C. Zhang, B. Anasori, A. Seral Ascaso, S. H. Park, N. McEvoy, A. Shmeliov, G. S. Duesberg, J. N. Coleman, Y. Gogotsi, V. Nicolosi, *Adv. Mater.* **2017**, *29*, 1702678.
- [39] P. B. Johnson, R. W. Christy, *Phys. Rev. B* **1972**, *6*, 4370.
- [40] M.-G. Kang, H. Joon Park, S. Hyun Ahn, L. Jay Guo, *Sol. Energy Mater. Sol. Cells* **2010**, *94*, 1179.
- [41] H. Y. Jang, S. K. Lee, S. H. Cho, J. H. Ahn, S. Park, *Chem. Mater.* **2013**, *25*, 3535.
- [42] J. Ou, J. Wang, D. Zhang, P. Zhang, S. Liu, P. Yan, B. Liu, S. Yang, *Colloids Surf., B* **2010**, *76*, 123.
- [43] Y. Li, W. Zhang, J. Hu, Y. Wang, X. Feng, W. Du, M. Guo, B. F. Liu, *Adv. Funct. Mater.* **2017**, *27*, 1606045.
- [44] E. M. Akinoglu, A. J. Morfa, M. Giersig, *Turk. J. Phys.* **2014**, *38*, 563.
- [45] L. Gao, F. Lemarchand, M. Lequime, *Quantum Semiclassical Opt.* **2013**, *8*, 603.
- [46] F. Abadizaman, S. Zollner, *J. Vac. Sci. Technol. B* **2019**, *37*, 062920.
- [47] J. R. DeVore, *J. Opt. Soc. Am.* **1951**, *41*, 416.